Computers and Chemical Engineering 93 (2016) 1–12

Contents lists available at ScienceDirect

Computers and Chemical Engineering

journal homepage: www.elsevier.com/locate/compchemeng

Dynamic operation of flat sheet desalination-membrane elements: A comprehensive model accounting for organic fouling

M. Kostoglou [a,*], A.J. Karabelas [b]

[a] Department of Chemistry, School of Chemistry, Aristotle University, Univ. Box 116, 541 24 Thessaloniki, Greece
[b] Chemical Process and Energy Resources Institute, Centre for Research and Technology—Hellas, P.O. Box 60361, 6th km Charilaou-Thermi Road, Thermi, Thessaloniki GR 570-01, Greece

ARTICLE INFO

Article history:
Received 1 April 2016
Received in revised form 30 May 2016
Accepted 2 June 2016
Available online 3 June 2016

Keywords:
Desalination
Reverse osmosis
Mathematical modeling
Organic fouling
Spiral wound membranes

ABSTRACT

Reliable simulation of membrane-module dynamic operation is essential in optimizing its detailed geometric characteristics and operation, as well as that of membrane plants, for various types of fluid treatment applications. This paper is part of systematic efforts toward development of such a comprehensive model, considering temporal variability caused by organic membrane fouling. To render the mathematical problem tractable, justified simplifications (retaining the physical parameter interdependencies) lead to a system of basic equations in two spatial planar coordinates, enabling to obtain a realistic temporal evolution of all process parameters. The flexible model structure allows integration of submodels, for phenomena occurring (and researched) at small spatial scales, which account for retentate spacer effects on friction losses and mass transfer, and constitutive expressions for fouling rates during desalination. The robust numerical algorithm developed to solve the system of differential and algebraic equations exhibits satisfactory convergence, appropriate for applications. The results presented herein demonstrate the versatility of the numerical code and its potential to analyze the interaction of mechanisms involved in fouling evolution, which is impossible by the much simpler one dimensional models. Directions for future developments are indicated.

1. Introduction

The very rapid expansion of membrane technology, in the past two decades, for various types of water treatment applications (e.g. desalination of brackish and sea water, effluent purification for reuse) has relied to a large extent on the use of flat-sheet spiral wound membrane (SWM) elements (Fritzmann et al., 2007; Greenlee et al., 2009). These SWM elements (well established in industry) facilitate the construction of rather flexible and *modular* desalination and water treatment plants, with production capacities that can vary at present in order of magnitude from 1 m^3/day to 10^6 m^3/day (e.g. Greenlee et al., 2009; Kurihara and Hanakawa 2013). The SWM modules are characterized by an ingenious design leading to high membrane packing density (in active membrane area per unit volume), which involves flat membrane sheets with thin spacers in-between (Karabelas, 2014) wrapped around a perforated central tube where the clean permeate is collected. The development of SWM modules to their presently marketable forms has been largely driven by the industrial needs, and facilitated by the accumulated technological experience over the years, with notable contributions from scientific research in the field of membrane materials (Elimelech and Phillip, 2011) as well as on membrane fouling and scaling and methods for their mitigation (Karabelas, 2014; Elimelech and Phillip, 2011). Moreover, it is well recognized that the complicated flow field in SWM modules and the spatially varying (even at steady state operation) process conditions are inadequately understood and modeled despite significant efforts especially during the past two decades (Karabelas et al., 2015). Recent relevant studies (Karabelas et al., 2014; Kostoglou and Karabelas 2013) and a state of the art review (Karabelas et al., 2015), regarding the effects of SWM module design parameters on its performance, show that significant progress has been made in developing a reliable steady-state simulator, and that a much needed for practical applications and research studies dynamic simulator (presently unavailable) requires a great deal of systematic development work. This study aims to contribute toward development of a comprehensive SWM dynamic simulator, by considering typical organic membrane fouling, which is a common cause for membrane plant temporal performance variability.

* Corresponding author.
E-mail address: kostoglu@chem.auth.gr (M. Kostoglou).

http://dx.doi.org/10.1016/j.compchemeng.2016.06.001
0098-1354/

The optimization of structural design, control and operation strategy of the membrane module requires the use of sufficiently detailed mathematical models in order to understand and quantify the interaction between the equipment design parameters and the process variables (Karabelas et al., 2015). A generalized mathematical modeling approach to membrane separation can be found in Marriott et al. (2001). However, the recent trend is to focus to specific details of each particular membrane process (Barello et al., 2015; Cao et al., 2016; Gurreri et al., 2016). Generally, the mathematical models can be of several degrees of complexity from simple integral (lumped parameter) to quite fundamental (first principles) approaches. However, the problem at hand is too complicated to allow a direct first principles approach; thus, a "divide and conquer" strategy is deemed necessary in order to handle efficiently several particular processes (sub-processes) occurring at different length and time scales. Specifically, the adopted approach is to derive constitutive expressions for the sub-processes based either on detailed subscale theoretical studies (wherever possible) or alternatively on experimental investigations for complex phenomena. Such an approach has been successfully followed in a previous publication (Kostoglou and Karabelas, 2013) for the development of a steady state SWM model, applicable to a clean membrane (i.e. no fouling occurring). The need to model the dynamic operation of SWM modules adds very significant complexity, i.e. the time varying module fouling must be accounted for. Four types of fouling are observed during SWM module operation: 1) scaling due to sparingly soluble salts (Hasson et al., 2001), 2) organic gel-layer formation (Schafer et al., 1998), 3) biofouling (Vrouwenvelder et al., 2009), 4) colloidal particle deposition (Yiantsios et al., 2005). The effect of the deposits is to increase the effective membrane resistance to permeation, to reduce the flow cross-sectional area in the retentate channels and to decrease the mobility of the solute, thus increasing concentration polarization. To systematically attack this problem, the present work is focused on the organic fouling which is the simplest to be modeled among the four fouling types. Therefore, the scope of this publication is to present the development of a dynamic model of SWM operation accounting for organic fouling, based on the previous steady state model (Kostoglou and Karabelas, 2013), and demonstrate its function as well as its capabilities; such a detailed dynamic model is unavailable at present. An ongoing assessment of the key system design and operating parameters on the SWM module dynamic performance (due to organic fouling) will be reported in a companion paper.

This paper is structured as follows: First, the model extensions with respect to the clean membrane case are discussed and the corresponding constitutive laws are suggested. Next, the dynamic model system of equations is presented and non-dimensionalized and the procedure for its solution is described. Finally, several characteristic model results are presented and discussed for two types of SWM-module operation, i.e. for steady state with a spatially non-uniform fouling layer and for dynamic module operation with a growing fouling layer.

2. Problem formulation

The dynamic model developed here is an extension of the steady state model presented in Kostoglou and Karabelas (2013), where the field variables are averaged in the transverse to the main flow direction, i.e. over the channel gap. The main features of the particular model include: (i) The capability to treat the two dimensionality of process parameters (throughout a membrane) induced by the finite pressure drop in the permeate channel, done in a detailed manner avoiding usual approximations (Schwinge et al., 2004; Avlonitis et al., 2007). (ii) The quasi-formal link to the equations describing in detail the transport process in the SWM module. (iii) The integration of sub-scale models and relevant expressions experimentally obtained in the authors laboratory. The model will be subsequently extended with the same degree of sophistication and in the same spirit of using appropriate subscale expressions based on detailed theoretical and experimental work. A first effort to simulate organic fouling evolution throughout a membrane sheet (Kostoglou and Karabelas, 2012) was restricted to the case of one-dimensional treatment of the retentate side and to the absence of solute to be separated from the feed. The results were encouraging, offering insights into the system dynamics and modeling issues, but the focus was not on model development leading to realistic simulation of SWM module operation.

The essential feature of the present model is the temporal variability of all process parameters caused by the growth of the organic fouling layer. Unlike the complexity of the other fouling modes, the mechanism of organic fouling appears to be rather straightforward. Indeed, the organic molecules are transferred to the membrane surface, aided by the normal permeation velocity, and adhere onto the membrane and further to the developing fouling layer. For major classes of foulants, it is realistic to consider *total* organic species rejection and no mass detachment (from the rather coherent fouling layer) by the shear stresses of the retentate cross-flow. Therefore, the local layer growth rate is taken proportional to the local permeate flux. Extensive experimental work performed in the authors laboratory (Sioutopoulos et al., 2010a,b) and elsewhere (e.g. Lee and Elimelech, 2006; Ye et al., 2005) shows that the above rather simple fouling mechanism can adequately describe reverse osmosis and nanofiltration membrane fouling by common organic matter, such as polysaccharides and their mixtures with humic acids. Further, there are several important issues, associated with the effect of a developing fouling layer on the SWM module performance, which should be examined (as follows) before proceeding with the derivation of the governing equations.

2.1. Extensions/Constitutive laws

The first issue concerns the *effect of the fouling layer on the pressure drop* in the retentate channel. The spacer filament diameter is denoted by D and it is by construction roughly equal to half of the retentate channel thickness. Assuming that the fouling layer has a uniform thickness h in the scale of the original *unit cell* (i.e. the elementary unit of the pattern formed by the crossing spacer filaments; Koutsou et al., 2007), a new unit cell must be considered in which the spacer-filaments exposed to flow will have cross sections of a circular segment (reduced by the part "immersed" in the fouling layer). However, the pressure drop relation for specified spacer type was determined by performing unit cell CFD simulations (in absence of fouling) and it was written in terms of a friction factor as f = f(Re) where Re is the Reynolds number based on D and on the local transversely averaged velocity (Koutsou et al., 2004; Koutsou et al., 2007; Ranade and Kumar, 2006). With a fouling layer, a new geometric parameter h/D should be added to the unit cell problem, and a modified constitutive relation of the form f = f(Re, h/D) is needed. In principle, such a relation can be determined by performing CFD simulations for several values of the parameters Re and h/D of the modified geometry. This type of simulations, involving a significant amount of work, will be performed in the future. At this stage an empirical closure of the constitutive relation will be pursued. For a clean membrane surface (h = 0), the relation between the retentate side pressure p and cross-flow velocity U is of the form (Kostoglou and Karabelas, 2009):

$$\frac{dp}{dx} = -\frac{f_1 U^{2-f_2} \rho^{1-f_2} \mu^{f_2}}{D^{1+f_2}} \tag{1}$$

where the dimensionless constants f_1 and f_2 depend on the type of the spacer (Koutsou et al., 2007). The constant f_2 takes values from 1

(purely viscous flow) to 0 (inertia dominated flow); the value $f_2 = 1$ corresponds to the case of channel with no inserts ("free-channel" case). The values of f_2 determined from the simulations for spacer-filled channels are between 0 and 1 (Koutsou et al., 2007), which are attributed to the strong effect of the spacer filaments on the pressure drop compared to the free-channel case. A simple approach to proceed (albeit approximate) is to replace the geometry by a channel of gap 2(D-h) and spacer filaments with circular cross section having a diameter (D-h); i.e. the effective filament cross section (which is a circular segment due to fouling) is replaced by a circular cross section of smaller diameter. The two spacer filaments (exact and approximate) have the same cross section normal to the flow (equal to D-h) whereas the areas of contact with the liquid are $(\pi\text{-}\cos^{-1}(1\text{–}2\,h/D))D$ and π(D-h), respectively. The pressure drop relation using the above approximation takes the form

$$\frac{dp}{dx} = -\frac{f_1 U^{2-f_2} \rho^{1-f_2} \mu^{f_2}}{(D-h)^{1+f_2}} \tag{2}$$

It is noted that for fixed flow rate the product U(D-h) must be constant and the pressure drop dependence on the channel gap is to the minus three power, irrespective of the f_2 exponent (spacer type). The above relation is only an approximation but it is a rational closure to the problem that remains to be validated (or improved) through detailed CFD simulations.

The second important issue regarding the organic fouling dynamics is the *reduction of membrane permeability* caused by the fouling layer or "cake" (as is usually referred to). The relation between wall normal velocity or flux u_w (units: m/s) and trans-membrane pressure Δp is commonly given as (Ruth, 1946):

$$u_w = \frac{1}{\mu(R_m + R_c)} \Delta p \tag{3}$$

Here R_m and R_c are the clean membrane resistance and the time-dependent fouling layer/cake resistance, respectively (units: m^{-1}). The latter is related to the deposit mass per surface area m (units: kg/m^2) through the relation $R_c = \alpha m$, where α is the specific cake resistance (units: m/kg). For the generally compressible cakes (as is the case of organic layers examined here), experiments show that α is proportional to $(\delta p)^n$ where δp is the difference between the applied pressure (retentate pressure) and a reference pressure and n is a compressibility exponent, i.e. $\alpha = \alpha_o(\delta p)^n$. The increase of the cake resistance due to compressibility effects may be attributed to the fact that part of the trans-membrane pressure is transformed to cake stresses, so the structure of the cake changes towards smaller porosity and smaller permeability. Several models exist in the literature to account for the structural variation across the cake thickness (e.g. Vorobiev, 2006). For cake filtration, the error of using the retentate pressure p without consideration of solid stresses to relate with α is discussed in Tien and Bai (2003). A simplification which offers a closure to the problem and it is supported by experimental data on flow resistance evolution for organic fouling layers is proposed in Kostoglou and Karabelas (2012) and Sioutopoulos et al. (2010a). According to this, the resistance α is a function of the pressure drop across the fouling layer i.e. $\alpha = \alpha_o(\Delta p - \mu R_m u_w)^n$. More recent extensive experimental campaigns of organic fouling of membranes in spacer-filled channels, for filtration under constant pressure and constant flux conditions, showed that the results can be adequately described by using the following rather simple constitutive law for the specific resistance α as a function of permeation flux $\alpha = \gamma u_w \beta$. The values of parameters (β, γ) depend on the type of foulant. The parameter β is dimensionless and the parameter γ has units: $m^{1-\beta} s^{\beta}/kg$. This is a major simplification (from the mathematical point of view) with respect to the previous approaches where the specific resistance is a function of wall flux, pressure and deposit thickness. The new constitutive relation holds locally for the relatively thin fouling layers (Karabelas and Sioutopoulos, 2014) developing on clean membranes; therefore, it is appropriate for simulating the evolution of organic deposits throughout the membrane sheets where the flux distribution is non-uniform. Nevertheless, additional research work is needed to enrich the database in support of this expression and to examine the sensitivity of fouling layer development to variation of the parameter (β, γ) values.

The existence of the fouling layer adds more complexity to the problem than simply considering resistance to fluid flow. For example, the fouling layer can alter the physico-chemical conditions responsible for scaling (Liu and Mi, 2012). Another complexity is the experimentally shown relation between layer permeability and solution ionic composition (Sioutopoulos et al., 2013). As more experimental results are added to the corresponding database, new interactions between the problem variables emerge. The simultaneous consideration of these interactions is not straightforward and this is another reason why comprehensive mathematical models are necessary, i.e. to enable transferring the results of the laboratory experiments to the industrial scale operation. At the present stage of model development, the interactions referred to above will not be considered; however, the so-called "cake enhanced concentration polarization" will be taken into account. This phenomenon was originally introduced to explain flux decline and rejection decrease during colloidal fouling of membranes (Hoek et al., 2002; Hoek and Elimelech, 2003). Here its analog for the case of organic fouling will be considered, based on the existence of the layer that prevents the back diffusion of the dissolved species thus increasing its concentration adjacent to the wall (concentration polarization). The following approach is taken to introduce the concentration polarization effect into the membrane model in the presence of spacers. At a location of the retentate channel, the transverse concentration profile is comprised of the uniform bulk concentration and a locally increased concentration in a region next to the membrane surface; this approach is referred to as "film theory" (Michaels, 1968). The wall region does not participate in the solute balances since the flow rate is small there. The wall concentration results from a balance between the wall flux (leading the solute to the wall) and the mass transfer process from the wall to the bulk (described by the corresponding mass transfer coefficient). The mass transfer coefficient can be determined from results of CFD simulations in the absence of wall flux; i.e. for non-porous walls (Koutsou et al., 2009). In order to retain the above framework, it is advantageous to consider cake-enhanced polarization as a mechanism essentially reducing the mass transfer coefficient. The modified mass transfer coefficient corresponds to the addition of two resistances in series outlined as follows. (i) Resistance to mass transfer through the cake for which the mass transfer coefficient is $k_{c1} = D_e/h$, where D_e is the effective diffusion coefficient in the fouling layer; the intrinsic diffusion coefficient of the solute is denoted as D_c and the ratio D_e/D_c is a quantity smaller than unity which depends on the layer internal structure. (ii) Resistance to mass transfer in the free part of the channel. As in the case of the pressure drop, a fundamental approach requires CFD simulations for mass transfer in the channel of reduced gap due to the development of the fouling layer. As a first approximation, the correlations for mass transfer coefficient derived for clean membranes (no fouling) can be employed. The only modifications made are the use of the increased velocity due to the reduced flow cross section and the reduction of the channel gap due to the developing fouling layer. This modification leads to a similar mass transfer coefficient for the clean and fouled channel for the same flow rate. Taking into account the above assumptions, the relation for the local mass transfer coefficient k_m (units: m/s) of the fouled channel is:

$$k_m = \left(\frac{h}{D_e} + \frac{D-h}{D_c g_1 Sc^{g_2} Re^{g_3}} \right)^{-1} \tag{4}$$

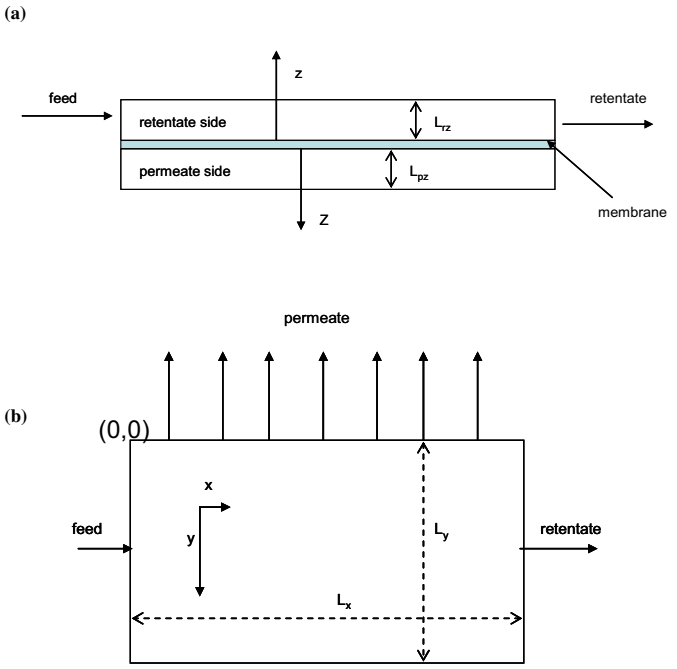

Fig. 1. Schematic of the membrane sheet; (a) cross-sectional view, (b) top view.

where Sc is the Schmidt number, Re is the local channel Reynolds number (using D-h as characteristic length) and the dimensionless parameters g_1, g_2, g_3 depend on the type of the spacer geometry (Koutsou et al., 2009).

2.2. Model equations

In this section the governing equations are presented which must be solved to determine the evolution of fouling and its effect on the membrane operation. The representative large length scale (entire membrane sheet) domain of computations treated here consists of half the retentate and the permeate channels, including the respective spacers, with the membrane in-between (Fig. 1). It is noted that in Fig. 1 not only the half but the whole width of the channels is shown. The dimensions of the membrane sheet are L_x and L_y whereas the gap of the permeate and retentate channel is L_{pz} and L_{rz}, respectively. The coordinate system considered is shown in Fig. 1; the two coordinates x,y are common for both permeate and retentate sides. The thickness of the retentate channel is twice the spacer filament diameter by construction (i.e. $L_{rz} = 2D$). As the fouling layer grows the "open" half-thickness of the channel is (D-h). Pointwise conservation equations are written for momentum and concentrations as in the case of steady state. The non-uniformity of h is assumed to be insignificant in the unit cell scale in order to achieve the appropriate closure. The macroscale equations are derived by taking averages across the channel gap.

Solving Eq. (2) for velocity and generalizing in vector form results in:

$$\vec{U} = -\left(\frac{(D-h)^{1+f_2}}{f_1 \rho^{1-f_2} \mu^{f_2}}\right)^{1/(2-f_2)} |\nabla p|^{(f_2-1)/(2-f_2)} \nabla p \tag{5}$$

To derive this expression it is considered that the velocity is almost unidirectional as it will be confirmed in the results section. The liquid mass balance in the retentate channel leads to the relation

$$\nabla \cdot (\vec{U}(D-h)) = -u_w \tag{6}$$

where u_w is the wall velocity or permeate flux and $\vec{U}$ is the retentate velocity vector field with components U_x and U_y.

The pressure – velocity relation in the permeate side is given as

$$\vec{u} = -\frac{k}{\mu} \nabla P \tag{7}$$

where k is the specific permeability of the permeate filler, $\vec{u}$ is the permeate velocity vector field with components u_x and u_y and P is the pressure at the permeate side.

The liquid mass balance for the permeate channel is the same as the one of the steady state case (which holds for all the permeate side equations) but it is implicitly dynamic in this case through the transient character of the wall flux; i.e.

$$\frac{1}{2} L_{pz} \nabla \cdot \vec{u} = u_w \tag{8}$$

The following notation is used for the several solute concentration variables employed here. The core (bulk) concentration of the retentate channel is denoted as C, the corresponding wall concentration as C_w and the permeate channel concentration as C_p. The units of all the concentrations are kg/m^3. The conservation equation for the core retentate concentration is given as

$$(D-h)\vec{U} \cdot \nabla C = u_w (C - (1-R)C_w) \tag{9}$$

Here R is the intrinsic rejection coefficient (dimensionless) which is a characteristic of the membrane. It is noted that in this work the rejection coefficient R is assumed to take a constant value; however, in general, R is a function of the local solute concentration and wall flux. The literature on such a relation is very extensive covering various degrees of sophistication from semi-empirical expressions (Wang et al., 2014) to detailed theories based on the Nernst-Planck and Poisson-Boltzmann equations (Wang et al., 1995; Hawkins Cwirko and Carbonell, 1998). Relaxing the simplification of constant R made here is a topic of parallel investigation.

The conservation equation for the permeate side solute concentration is

$$\frac{L_{pz}}{2} \vec{u} \cdot \nabla C_p = u_w ((1-R)C_w - C_p) \tag{10}$$

The wall solute concentration is related to the local core concentration according to the following relation, including concentration polarization effects (Kostoglou and Karabelas, 2013):

$$C_w = C/(1 - R + Re^{-u_w/k_m}) \tag{11}$$

It is noted that for these effects different expressions can be found in the literature due to different application of the film theory (Lyster and Cohen, 2007; Guillen and Hoek, 2009). However, the results using different expressions are very similar for the common case of large rejection values and relatively small concentration polarization, as is the case here. The mass transfer coefficient k_m is given by Eq. (4). The following relation is obtained for the wall flux, using the expression proposed in Karabelas and Sioutopoulos (2014) for the developing fouling resistance

$$u_w = \frac{p - P - \Gamma(C_w - C_p)}{\mu(R_m + \gamma u_w^{\beta} m)} \tag{12}$$

where Γ is the so-called osmotic coefficient and the parameters γ, β have been previously discussed. The evolution of the fouling layer mass density is given by the simple equation:

$$\frac{dm}{dt} = u_w C_f \tag{13}$$

where t is the filtration time (starting from a clean membrane) and C_f the concentration of the foulant assumed to be spatially uniform and equal to its inlet value. The fouling layer thickness is related to the mass m through $h = m/\rho_f$ where ρ_f is the density of the layer. The physical boundary conditions are the inlet retentate pressure p_{in}, the outlet retentate pressure p_{out}, the zero retentate-channel velocity U_y at $y = 0$ and $y = L_y$, the given inlet solute concentration

C_o and the inlet foulant concentration C_f. The permeate channel boundary conditions are the reference pressure P = 0 at y = 0 and the zero normal velocity at $y = L_y$, x = 0 and $x = L_x$. The mathematical problem is always solved using the above type of boundary conditions. The real system boundary conditions (prevailing during membrane operation), of a fixed flow-rate and a fixed permeate recovery, appear as integral constraints which must be satisfied by choosing appropriately p_{out} and p_{in} values.

2.3. Non-Dimensionalization

The final system of equations is non-dimensionalized in order to reduce the number of problem parameters. The specific non-dimensionalization scheme proposed in the present work was found to facilitate the chosen numerical solution strategy. Specifically, all lengths are normalized with the membrane length L_x, pressures are normalized with the inlet pressure p_{in}, the solute concentrations with the inlet solute concentration C_o and the fouling layer thickness with the spacer-filament diameter D. The channel velocities are normalized with the reference velocity U_o (denoting the velocity for zero outlet pressure) given as

$$U_o = \left(\frac{D^{1+f_2}}{f_1 \rho^{1-f_2} \mu^{f_2}} \frac{p_{in}}{L_x} \right)^{1/(2-f_2)} \tag{14}$$

The wall flux is normalized with the reference flux u_{wo} (denoting wall flux in the absence of permeate pressure drop and of osmosis) commonly represented by

$$u_{wo} = \frac{p_{in}}{R_m \mu} \tag{15}$$

No new symbols will be introduced for the dimensionless variables for clarity of presentation. The governing equations are:

$$\frac{\partial}{\partial x}(1-h)^{3/(2-f_2)} \left[\left(\frac{\partial p}{\partial x} \right)^2 + \left(\frac{\partial p}{\partial y} \right)^2 \right]^{0.5\varepsilon} \frac{\partial p}{\partial x} + \frac{\partial}{\partial y}(1-h)^{3/(2-f_2)} \left[\left(\frac{\partial p}{\partial x} \right)^2 + \left(\frac{\partial p}{\partial y} \right)^2 \right]^{0.5\varepsilon} \frac{\partial p}{\partial y} = A u_w \tag{16}$$

$$\frac{\partial^2 P}{\partial x^2} + \frac{\partial^2 P}{\partial y^2} = B u_w \tag{17}$$

$$(1-h)\left(U_x \frac{\partial C}{\partial x} + U_y \frac{\partial C}{\partial y} \right) = A u_w (C - (1-R) C_w) \tag{18}$$

$$\frac{\partial P}{\partial x}\frac{\partial C_p}{\partial x} + \frac{\partial P}{\partial y}\frac{\partial C_p}{\partial y} = B u_w (C_p - (1-R) C_w) \tag{19}$$

$$c_w = C/(1 - R + R \cdot e^{-Eu_w/[(U_x^2+U_y^2)^{g_3/2}(1-h)^{g_3-1}](1+\Lambda(U_x^2+U_y^2)^{g_3/2}(1-h)^{g_3-1})}) \tag{20}$$

$$u_w = \frac{p - P - G(C_w - C_p)}{1 + H u_w^{\beta} h} \tag{21}$$

$$u_{px} = -\frac{A}{B}\frac{\partial P}{\partial x} \tag{22a}$$

$$u_{py} = -\frac{A}{B}\frac{\partial P}{\partial y} \tag{22b}$$

$$U_x = -(1-h)^{(1+f_2)/(2-f_2)} \left[\left(\frac{\partial p}{\partial x} \right)^2 + \left(\frac{\partial p}{\partial y} \right)^2 \right]^{0.5\varepsilon} \frac{\partial p}{\partial x} \tag{23a}$$

$$U_y = -(1-h)^{(1+f_2)/(2-f_2)} \left[\left(\frac{\partial p}{\partial x} \right)^2 + \left(\frac{\partial p}{\partial y} \right)^2 \right]^{0.5\varepsilon} \frac{\partial p}{\partial y} \tag{23b}$$

The boundary conditions for the above system of partial differential equations are

$$\frac{\partial p}{\partial y} = 0 \quad \text{at} \quad y = 0,\ y = L_y \tag{24a}$$

$$\frac{\partial P}{\partial y} = 0 \quad \text{at} \quad y = L_y \tag{24b}$$

$$\frac{\partial P}{\partial x} = 0 \quad \text{at} \quad x = 0,\ x = 1 \tag{24c}$$

$$P = 0 \quad \text{at} \quad y = 0 \tag{24d}$$

$$p = 1 \quad \text{at} \quad x = 0 \tag{24e}$$

$$p = p_{out} \quad \text{at} \quad x = 1 \tag{24f}$$

$$C = 1 \text{at} x = 0 \tag{24g}$$

The dimensionless parameters appearing in the above equations are defined as

$$A = \frac{2L_x u_{wo}}{U_o L_{rz}},\ B = \frac{2L_x^2}{k R_m L_{pz}},\ G = \frac{\Gamma C_o}{p_{in}},\ E = \frac{D u_{wo}}{D_c g_1 Sc^{g_2} Re_o^{g_3}},\ \varepsilon = \frac{f_2 - 1}{2 - f_2}$$

$$\Lambda = \frac{D_c g_1 Sc^{g_2} Re_o^{g_3}}{D_e},\ H = \frac{\gamma u_{wo}^{\beta} \rho_f D}{R_m}$$

where Re_o is the Reynolds number corresponding to velocity U_o. These dimensionless parameters provide a measure of the magnitude of the following physical quantitiesA: permeate recovery,B: pressure drop in the permeateG: osmotic pressureE: concentration polarizationH: fouling layer resistanceΛ: cake-enhanced concentration polarization.

The boundary conditions (24e,f) correspond to constant in time inlet pressure and solute concentration. Their extension for time dependent inputs is trivial; i.e. p = p_{in}(t), C = C_o(t). In that case the normalization values are $p_{in}(0)$ and $C_o(0)$.

Some integral quantities of particular interest are computed as follows. The flow rate must be used as input variable instead of velocity since the velocity depends on the local deposit thickness. The reference flow rate Q_o (per membrane sheet) is defined as $Q_o = 2U_o L_y D$. The inlet flow rate normalized with respect to Q_o can be computed as

$$Q = \frac{1}{L_y}\int_0^{L_y} U_x(0,y)(1 - h(0,y))dy \tag{26}$$

The recovery ratio F which denotes the fraction of the inlet flow that goes to permeate is computed as

$$F = \frac{A}{QL_y}\int_0^{L_y}\int_0^{1} u_w dx dy \tag{27}$$

Finally, the average (mixing-cup) solute concentration in the permeate is given as

$$C_{p,ave} = \int_0^{L_y}\int_0^{1} C_p u_w dx dy \Big/ \int_0^{L_y}\int_0^{1} u_w dx dy \tag{28}$$

The effective (observed) solute rejection coefficient is defined as $R_{eff} = 1\text{-}C_{p,ave}$.

A crucial point in the derivation of the evolution equation is the choice of the average deposit thickness as pseudo-time variable. This allows the numerical integration to proceed on a physically sound basis, i.e. the time step corresponds to a certain degree of deposit growth avoiding waste of computational resources by employing time steps with no considerable variables evolution. Let us call τ the average deposit thickness. The deposit evolution equation takes the form

$$\frac{dh}{d\tau} = \frac{L_y u_w}{\int_0^{L_y}\int_0^1 u_w dy dx} \tag{29}$$

The actual time t normalized by the reference time $t_o = D\rho_f/(u_{wo}C_f)$ can be obtained as a function of the average deposit thickness from the equation:

$$\frac{dt}{d\tau} = \frac{L_y}{\int_0^{L_y}\int_0^1 u_w dy dx} \tag{30}$$

The direct solution of the above problem leads to the computation of functions Q(t) and F(t) for given $p_{in}(t)$ and $p_{out}(t)$. In order to simulate membrane operation of practical interest, either for the case of constant pressure or constant flux, the role of parameters Q(t), $p_{out}(t)$, F and p_{in} as input and output variables should be appropriately assigned.

2.4. Solution technique

The system of Eqs. (16)–(23) and (29)–(30) with boundary conditions (24) has to be solved. The solution algorithm employed is very robust and unconditionally stable. The time discretization is based on the simple explicit Euler method. The particular normalization of the equations used, allows a relatively small number of discretization steps, because only steps with essential variable advancement are implemented. The partial differential equations and the corresponding boundary conditions are discretized using second order finite differences. Eqs. (18), (19) are discretized using upwind first order finite differences due to their strong convective character. The system of equations is solved using an iterative (Gauss-Seidel) scheme. The non-linear pair of Eqs. (20), (21) is solved for each spatial position by a combination of bisection and Newton-Raphson method. For the constant pressure case, searching for a p_{out} value that leads to a given flow rate is embodied in the iteration process. The starting values for iteration are crucial for the stability of the algorithm; thus, an analytical prediction for p_{out} in the limit of zero recovery is used as starting value. The situation is more complicated in the constant flux case, where the secant method is used in each time step to determine the p_{in} value that leads to the required flux.

3. Results and discussion

The results presented here are intended to show the robustness of the algorithm in solving the equations, and to demonstrate the multitude of useful output data. Whereas realistic values are chosen for most of the parameters, rather extreme values are selected for some of them in order to exaggerate some phenomena (as concentration polarization, pressure drop in the retentate, pressure drop in the permeate side) and to demonstrate their interaction. Consequently, some of these results are not representative of practical applications. Two types of simulations are presented here. The first type refers to *steady state operation of a fouled membrane* with inlet pressure and inlet flow rate fixed; several uniform or non-uniform shapes are assumed for the organic layer in order to assess the influence of its non-uniformity on the membrane operation. The second type of simulations deals with the *growth of an organic fouling layer* on an initially clean filtration membrane; results for the common operating modes of constant inlet pressure and constant permeate flux are presented. The total inlet flow rate is considered constant for both modes.

The parameter values chosen to designate a *reference case* are A = 0.1, $\varepsilon = -0.4$, $L_y = 1$ (square membrane sheet), B = 1, E = 0.5, $g_3 = 0.7$, $\Gamma = 0.2$, R = 0.99, $U_o = 0.2$, $\beta = 1$. The exponents ε and g_3 correspond to results obtained from unit cell CFD simulations of real spacer structures (Press et al., 1992), whereas the exponent β is in the range proposed based on the experimental data from this laboratory (Karabelas and Sioutopoulos, 2014). Regarding the magnitude of the other parameter values, the used dimensionless flow rate U_o leads to a pressure drop of about 5% which is rather high, the parameter B value leads to a permeate pressure drop contribution to the total pressure difference of about 20% which is also high, but the rest of the parameter values correspond to practical conditions of membrane operation.

The results of the steady state simulations are presented first. **Case I** corresponds to the clean membrane (h = 0 throughout) and it is used as reference. In all other cases a fouling layer is considered to exist with an average thickness $h_{ave} = 0.1$. In **case VI** the layer thickness is uniform throughout the membrane, whereas in the other four cases there is a linear variation from h = 0 to h = 0.2 in one direction for each case. Specifically, the variation from h = 0 to h = 0.2 is in the positive y-direction in **case II**, in the negative y-direction in **case III**, in the positive x-direction in **case IV** and in the negative x-direction in **case V**.

At first it is assumed that the fouling layer has no influence on the wall flux (i.e. H = 0). This is of course not realistic but the scope is to study the effect of retentate flow cross section non-uniformity on the membrane operation. The dimensionless retentate x-velocity U_x profiles are shown in Fig. 2(a) and (b) along the lines y = 0 and $y = L_y$, respectively. The velocity profile is dominated by three competing contributions: (i) reduction of the flow rate due to the flow loss to the permeate through the membrane; (ii) increase of velocity due to the flow cross-section reduction caused by the fouling layer; (iii) redistribution of the flow in the y direction in order to satisfy pressure requirements. The velocity decrease in case I is simply due to the flow rate reduction. The velocity at x = 0 (inlet velocity) is increased in all cases (except case IV) due to the existence of the fouling layer. Case VI shows an almost parallel shift of the clean membrane (Case I) profiles; the velocity increase in case VI is simply due to the cross-sectional area reduction. The case IV is of particular interest; i. e. the flow rate reduction along the membrane is totally counterbalanced by the cross section decrease leading to a more or less uniform velocity in the retentate side of the membrane channel. On the other hand, in case V the axial flow rate reduction and the cross section increase along the flow have a synergistic effect leading to enhanced velocity reduction. The velocity profiles for the cases II and III are rather unexpected; i.e. the two velocities are larger at the side of lower fouling layer thickness, which is due to the flow redistribution. Indeed, the pressure drop is a non-linear function of the channel thickness (as it has been already discussed) so it is much larger in the region of high fouling layer thickness h; thus, the flow is redistributed toward regions of low h for pressure equilibration. This counterintuitive relative magnitude of profiles II and III in Fig. 2(a) and (b) is the opposite from what is predicted by a simplified one-dimensional model for the retentate side.

The main pressure equilibration mechanism is the redistribution of the inlet flow with respect to y-coordinate. Nevertheless,

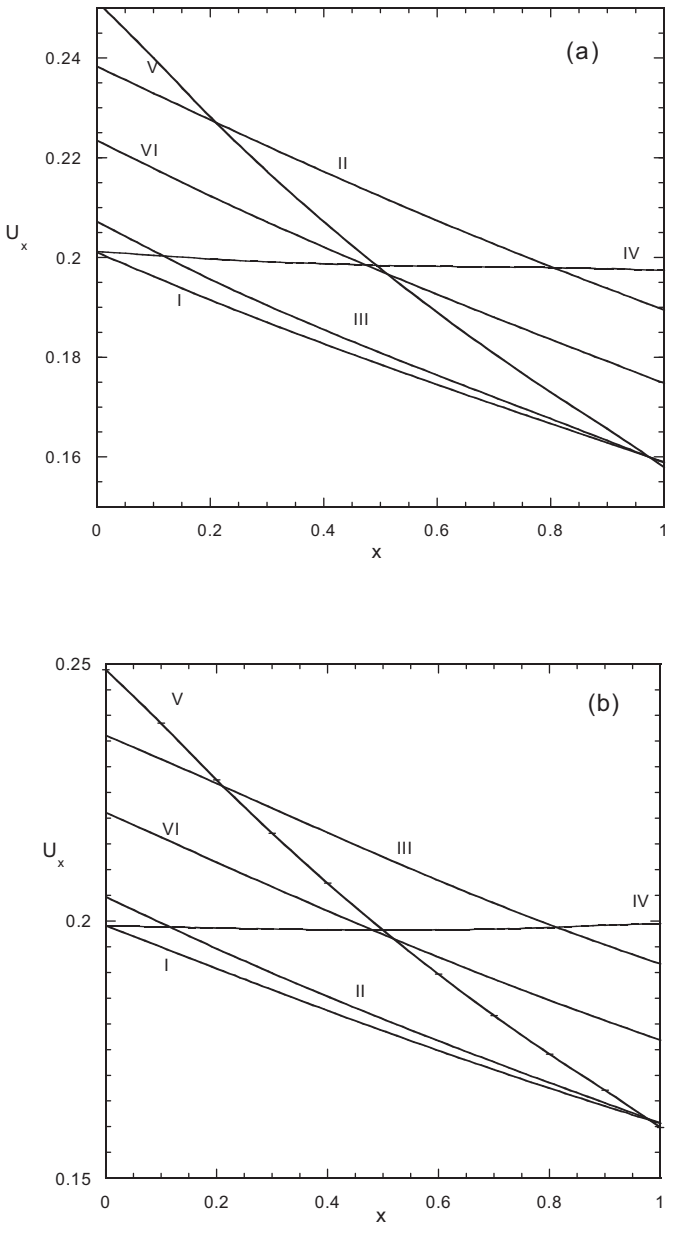

Fig. 2. Retentate side x-component of velocity U_x variation in the x-direction, for cases I to VI; (a) at y = 0, (b) at y = 1.

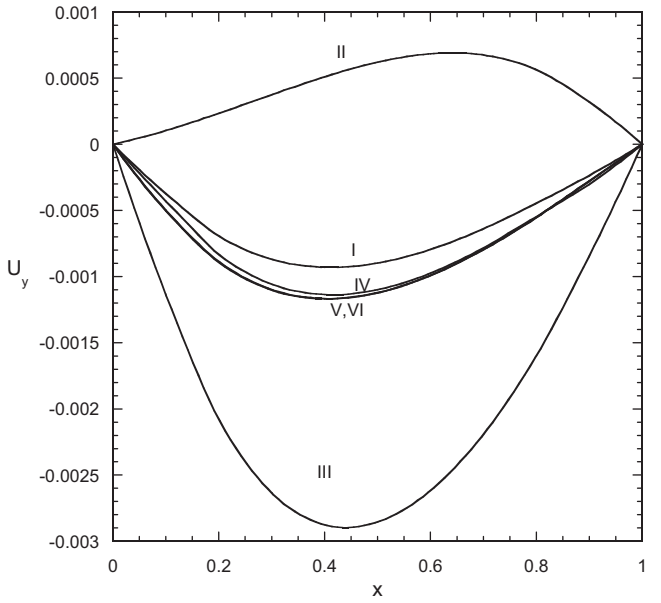

Fig. 3. Retentate side y-component of velocity U_y variation in the x-direction at y = 0.5, for cases I to VI.

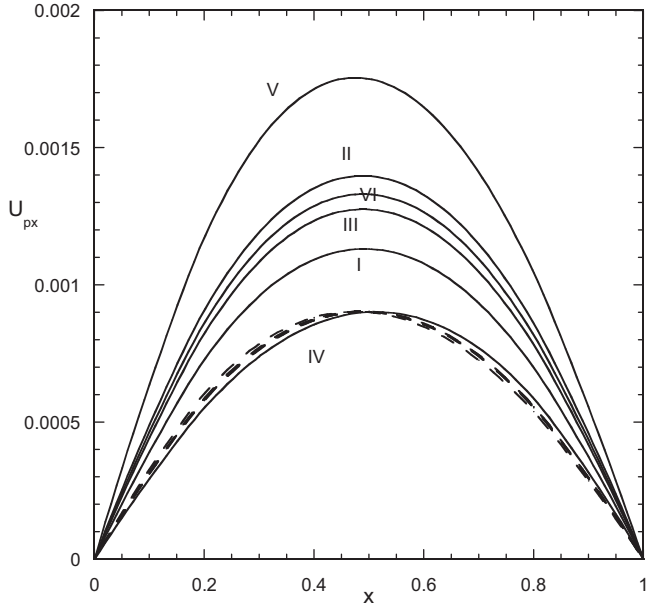

Fig. 4. Permeate side x-component of velocity U_{px} variation in the x-direction at y = 1, for several cases (continuous lines). The curves for cases I, II, III, V, VI are also shown normalized to have the same maximum with the curve for case IV (dashed lines).

small flow adjustments along the retentate channel are possible through the velocity U_y. Axial (x-direction) profiles of this velocity for y = 0.5 are shown in Fig. 3; in general the U_y values are very small. The participation in the water mass balance is through its y-derivative and the flow adjustments are of localized nature. The velocity for clean membrane (case I) is negative because the loss to permeate is higher towards line y = 0 (larger trans-membrane pressure) so the flow goes from high to small y regions. The U_y profiles for cases IV, V, VI are very similar to the one of case I. This is expected since the fouling layer is uniform in the y-direction in those cases. On the contrary, in case III the flow towards smaller y is of increased magnitude, whereas in case II the component U_y changes direction from small to high y values. The pressure equilibration requirement leads to a practically one dimensional pressure profile. Despite this trend the resulting retentate velocity distribution is not one-dimensional.

The velocities shown in Fig. 3 were obtained by assuming that the pressure drop relation is the same for both x and y directions; this assumption has been extensively discussed in Kostoglou and Karabelas (2009). According to the present results, the velocity may not be uniform in the y direction but its angle with the x-axis is typically smaller than one degree; therefore, the assumption does not influence the macroscopic model results but may have an effect on secondary fields like U_y. Another secondary field not considered by conventional models is the x direction velocity in the permeate U_{px}. The profiles of U_{px} versus x at y = 1 are shown in Fig. 4. It is interesting that the shape of the profile is almost independent of the problem parameters even for the strong non-uniformities appearing in the present case. The profiles normalized with respect to their maximum values appear to merge into a single curve as it is shown in Fig. 4.

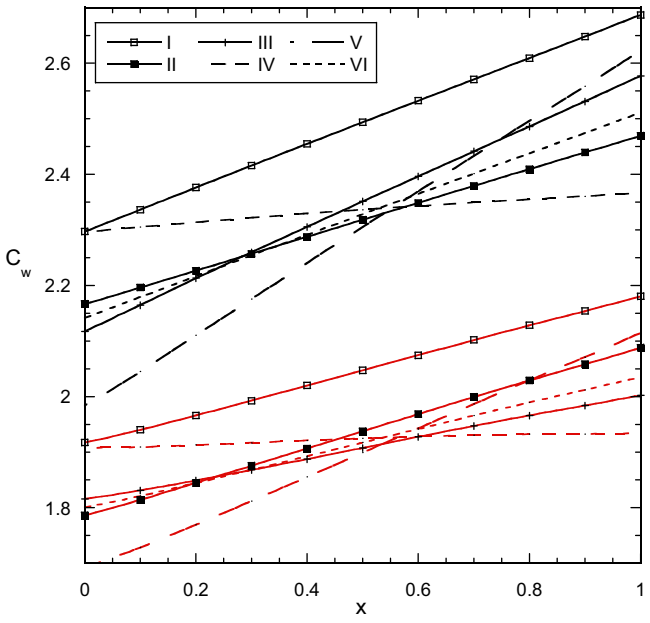

Fig. 5. Retentate side wall concentration C_w variation in the x-direction for cases I to VI. The upper family of curves (black lines) corresponds to y = 0 and the lower family (red lines) to y = 1 (for interpretation of the references to colour in this figure legend, the reader is referred to the web version of this article).

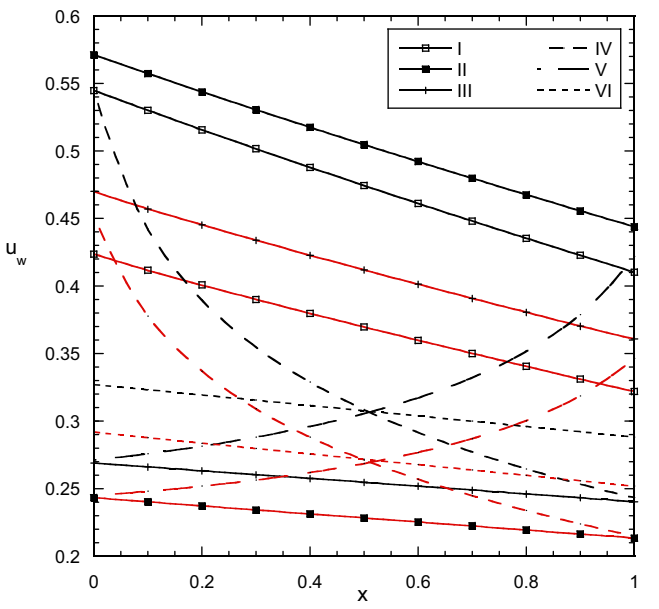

Fig. 6. Wall flux u_w variation in the x-direction for cases I to VI with H = 60, at y = 0 (black lines) and y = 1 (red lines). The curve with higher values for each case corresponds to y = 0 except in case III which corresponds to y = 1 (for interpretation of the references to colour in this figure legend, the reader is referred to the web version of this article).

The retentate wall concentration C_w profiles in the x direction are shown in Fig. 5 for y = 0 and y = 1. To interpret these profiles, it is recalled that the local fluxes are larger at y = 0, so the concentration polarization leads to larger concentration values there. In general, the existence of the fouling layer increases the local velocities compared to the clean membrane case so the mass transfer coefficient is increased and the concentration polarization tends to be reduced. In case IV, both wall flux u_w and mass transfer coefficient increase in the x direction leading to almost uniform wall concentration. The situation is different in case V where the mass transfer coefficient decreases in the x-direction leading to increased concentration polarization. The C_w profiles are similar in the cases II, III and VI for which there is no fouling layer non-uniformity in the x-direction.

Computational results plotted in the next two Figs. 6 and 7 correspond to the more realistic case of trans-membrane pressure reduction due to the fouling layer. The value H = 60 is considered, corresponding to 20% flux reduction for $h_{ave} = 0.1$. The scope here is to show the effect of the layer non-uniformity on such process parameters as the wall flux and the output concentration that are sensitive to the fouling-layer permeability. Fig. 6 depicts the wall flux u_w profiles along the x coordinate for y = 0 and y = 1, for the cases I–VI with deposits. In most cases the flux tends to almost linearly decrease along the x-coordinate due to retentate pressure drop (reduced driving force). The cases IV and V differ in that the deposit resistance to permeation varies in the x direction. The wall flux in case IV tends to non-linearly decrease along the flow, whereas in case V the increase of deposit resistance overcomes the pressure decrease. The wall flux in most cases is increased for small y due to smaller permeate pressure. This trend is enhanced in case II and is reversed in case III due to the y direction non-uniformities of the fouling layer.

The profile of the solute concentration at the outlet of the permeate side (y = 0) of the membrane is shown in Fig. 7. In general, the mixing through the flow in the x-direction in the permeate side is quite insignificant whereas there is considerable mixing in the y-direction. Considering these trends, one could say that the concentrations in Fig. 7 are representative of properly y-averaged (for each value of x-coordinate) permeate concentrations. Fig. 7 shows that there is an almost linear increase of permeate-concentration in the x direction in cases I–III, VI; this implies that the effect of increasing retentate concentration along the flow overcomes that of reduced wall flux, thus leading to increased wall concentration. The wall flux is smaller in the presence of fouling layer, so the concentration polarization is reduced and this explains the different magnitude of the permeate concentration for the above cases. For cases IV and V, the large variation of wall flux along the flow leads to corresponding variation of the retentate wall concentration and of the outlet permeate concentration shown in Fig. 7.

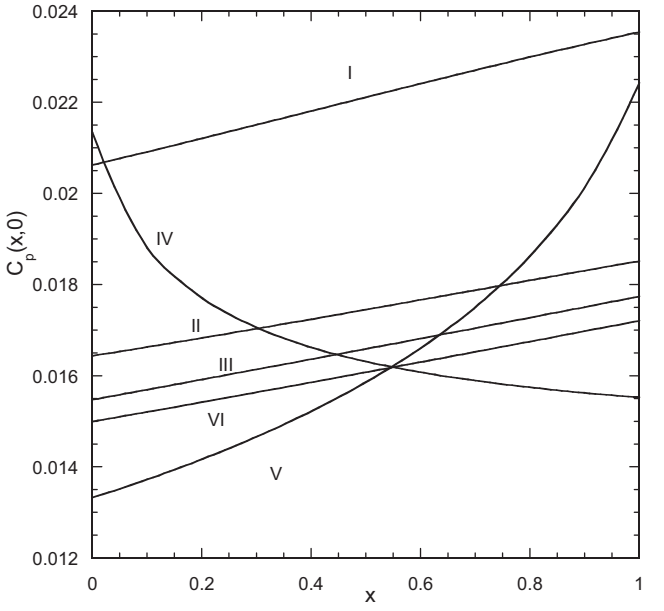

Fig. 7. Variation of outlet permeate concentration C_p (at y = 0) along coordinate x for cases I to VI (H = 60).

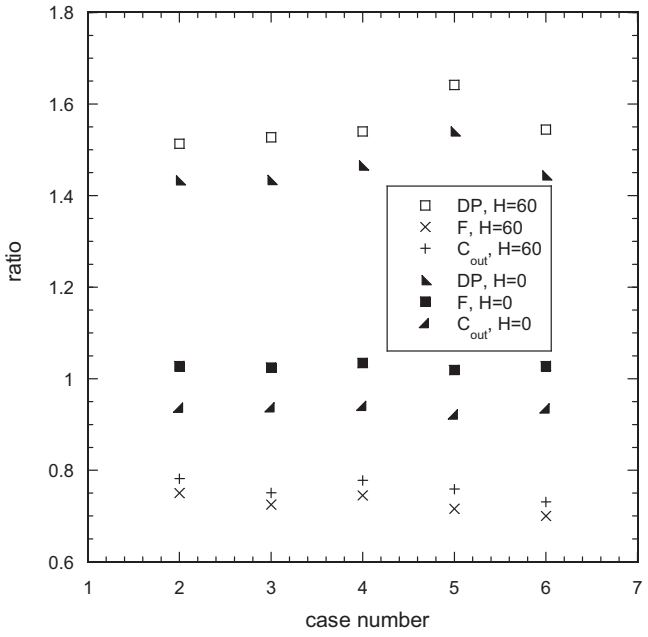

Fig. 8. Ratio of pressure drop DP, recovery ratio F and outlet concentration C_{out} for cases II–VI (represented with the numbers 2–6) over the corresponding values for case I (clean membrane), for H = 0 and H = 60.

Some global measures for the cases examined are presented in Fig. 8. For clarity of presentation only the ratios of each variable to the corresponding clean membrane variable are presented. The pressure drop DP is very significantly increased in the presence of deposit due to the reduction of the flow cross section, which is accounted for by the pressure drop expression considered here. The pressure drop is larger for H = 60 than for H = 0 because the total flow passing through the retentate channel is greater in the former case (smaller recovery). There is no actual difference in pressure drop between the different cases except for case V; in the latter the pressure drop is increased because the flow restriction is in the region of high flow rate leading to very high local velocities. The normalized recovery ratio F is slightly greater than 1 for H = 0 because the flow restriction due to fouling leads to higher velocities and higher mass transfer coefficients, thus reducing concentration polarization. Much smaller recovery F values are obtained for H = 60 due to the reduction of the wall flux. The output permeate concentration C_{out} (which is identical to $C_{p,ave}$) follows the pattern of recovery ratio regarding the differences between the cases. The level of this output concentration is smaller for H = 60, compared to H = 0, due to the relatively smaller wall flux that leads to reduced concentration polarization.

The second part of the results deals with the dynamic process simulations of initially clean membranes. Some typical deposit evolution profile data for the base case with H = 60 and $\Lambda = 0$ (no "cake-enhanced" concentration polarization) will be presented first. A sequence of fouling layer thickness profiles for *constant inlet pressure* is presented in Fig. 9(a) for y = 0 and y = 1. Although it is not clear in this figure, the *relative* non-uniformity of the profile decreases as the thickness increases due to the self-regulating character of the growth process. The corresponding wall flux profiles depicted in Fig. 9(b) show that the flux decreases as the fouling layer grows. The flux and the fouling layer thickness decrease along the flow as well as with increasing y. The fouling layer profile evolution for the case of simulation *under constant flux* conditions is shown in Fig. 10(a). In general, the tendency for suppression of thickness non-uniformities is greater for constant flux than for constant pressure conditions. The evolution of the wall flux profiles is shown in

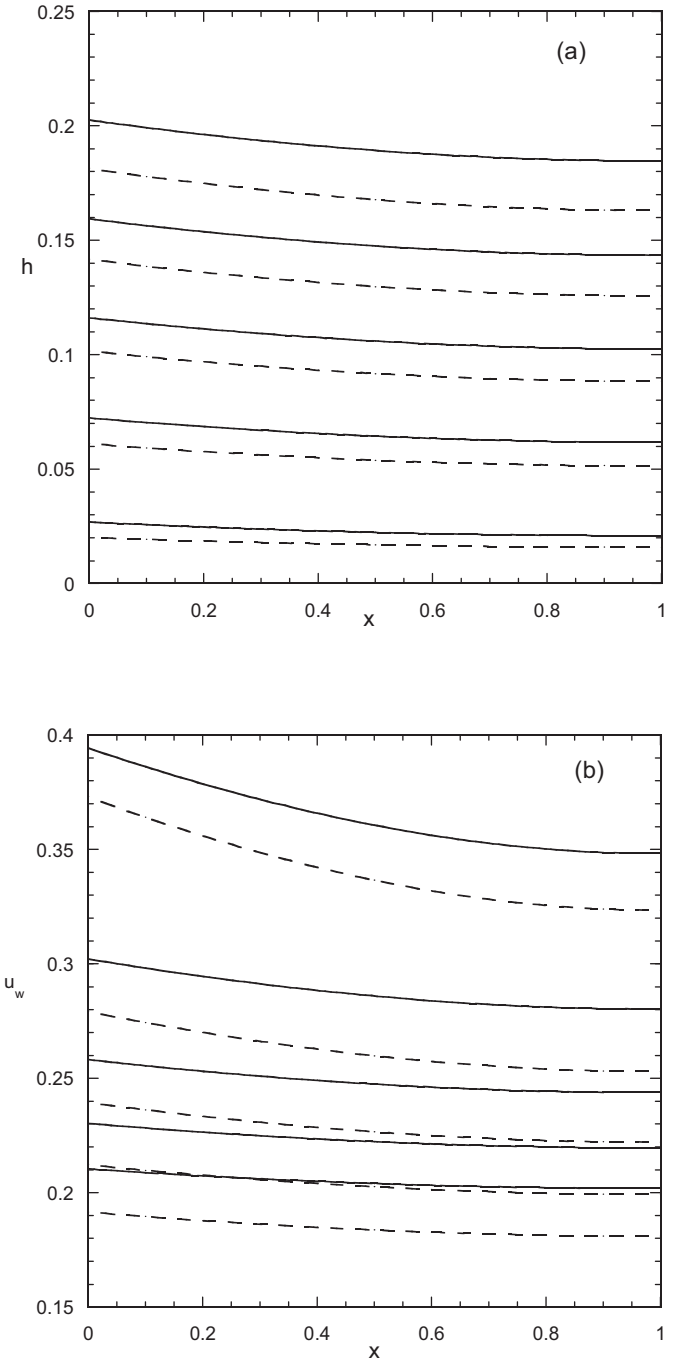

Fig. 9. Evolution of (a) fouling layer thickness and (b) wall flux profiles along the x coordinate for constant inlet pressure (H = 60). The solid lines correspond to y = 0 and the dashed lines to y = 1. As time proceeds fouling layer thickness increases and wall flux decreases.

Fig. 10(b) where the tendency to evolve towards a uniform wall flux is evident.

The evolution is presented next of some integral quantities and some field non-uniformities during the dynamic operation of the initially clean membrane under constant pressure and constant flux conditions. Three cases are considered: **case A** (H = 60, $\Lambda = 0$) with only fouling layer resistance reducing wall flux, **case B** (H = 0, $\Lambda = 50$) with only cake-enhanced concentration polarization, and **case C** (H = 60, $\Lambda = 50$) with both these inhibition mechanisms involved. The evolution of the flow recovery and product concentration for the constant pressure operation is shown in Fig. 11;

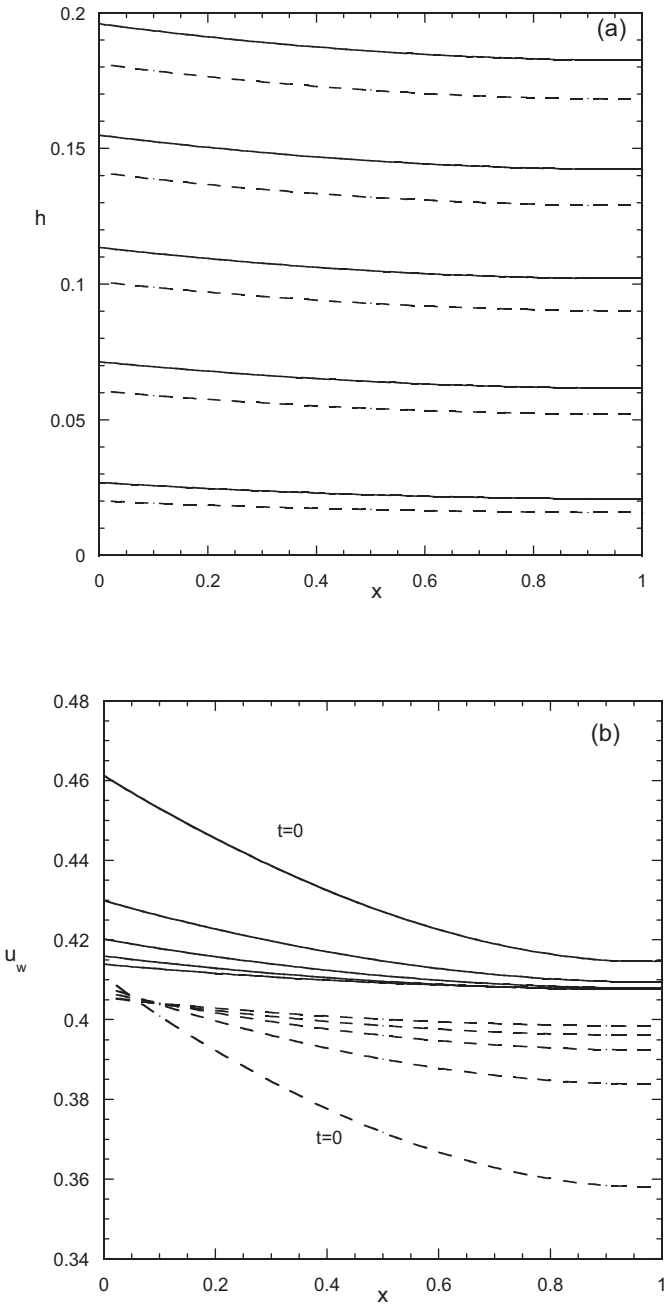

Fig. 10. Evolution of (a) fouling layer thickness h and (b) wall flux profiles in x coordinate for constant total flux (H = 60). The solid lines correspond to y = 0 and the dashed lines to y = 1. As time proceeds, fouling layer thickness increases and wall flux tends asymptotically to uniform shape.

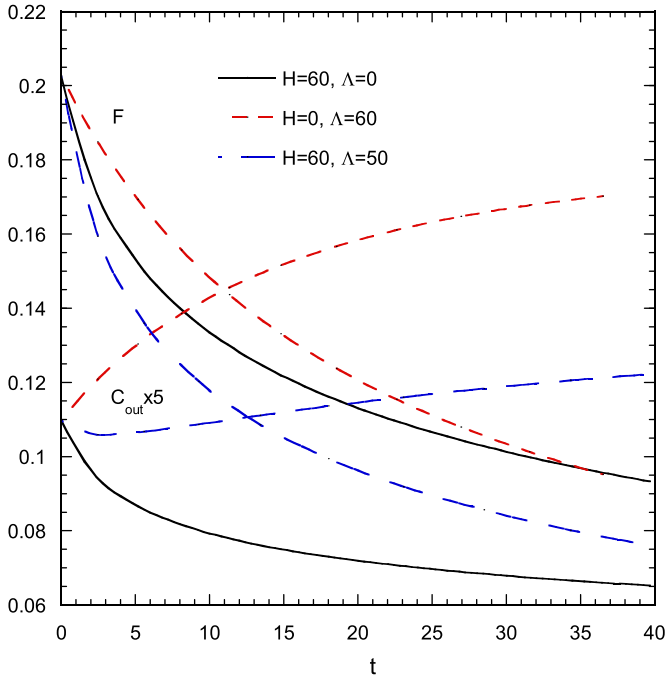

Fig. 11. Evolution of flow recovery F and outlet solute concentration C_{out} (×5 for clarity) for three combinations of parameters H, Λ; *constant pressure operation.*

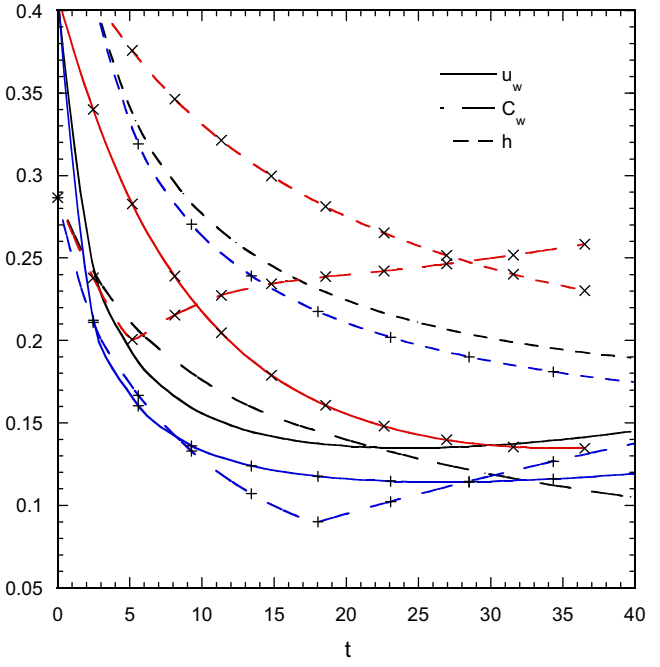

Fig. 12. Evolution of the maximum fractional non-uniformity for wall flux u_w, wall concentration C_w and deposit thickness h for three combinations of parameters H, Λ. The simple lines are for H = 60, Λ = 0, the lines marked with "x" correspond to H = 0, Λ = 50 and lines marked with "+" correspond to H = 60, Λ = 50: *constant pressure operation.*

the recovery decreases with time, as expected. The initial decrease is faster for case A than for case B but after some time the two curves cross each other; this is due to the different mechanisms of permeation-flux reduction in the two cases. The recovery is larger in case C where both inhibition mechanisms are present. The product concentration reduction in time in case A is due to the decrease of the wall flux that leads to reduced concentration polarization. The situation is more complicated in cases B and C; cake enhanced concentration polarization leads to reduction of the mobility of the solute which competes with reduction of the wall flux. This competition leads to increase of product concentration in time for case B and to an almost constant product concentration for case C, where solute mobility reduction counterbalances wall flux reduction.

Fig. 12 depicts the evolution of the maximum fractional non-uniformity from the mean in the x-y plane for wall flux, retentate wall concentration and fouling layer thickness. The simulations for both constant pressure and constant flux operation modes are performed up to mean thickness h_{ave} = 0.2. It is reminded that the time to achieve this thickness is larger for constant pressure than for the constant flux case. The thickness non-uniformity decreases with time in all cases. The wall concentration non-uniformity decreases

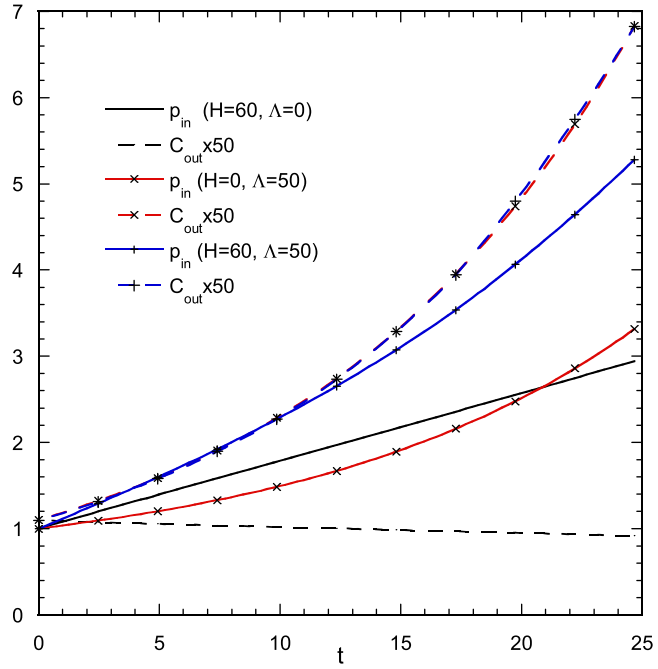

Fig. 13. Evolution of membrane inlet pressure p_{in} and outlet permeate concentration C_{out} (x50 for clarity) for three combinations of parameters H and Λ: *constant mean flux operation.*

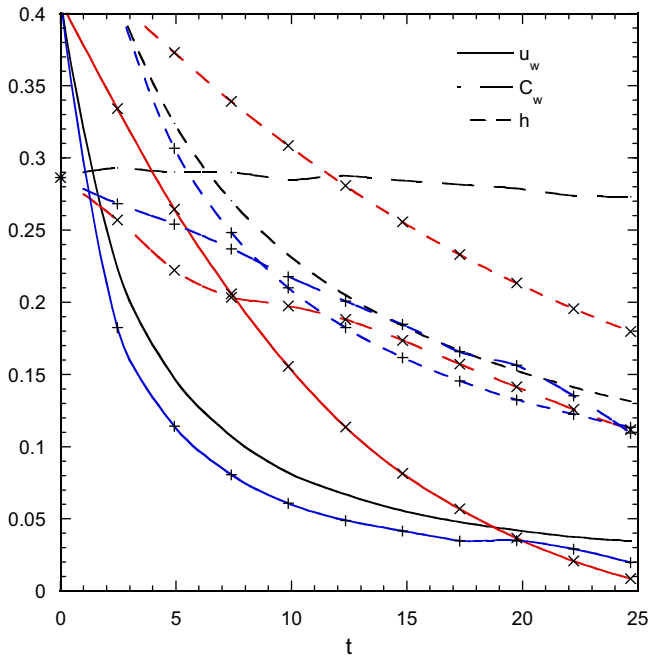

Fig. 14. Evolution of the maximum fractional non-uniformity for wall flux u_w, wall concentration C_w and deposit thickness h, for three combinations of parameters H, Λ. The simple lines are for H = 60, Λ = 0, the lines with "x" are for H = 0, Λ = 50 and the lines with "+" are for H = 60, Λ = 50: *constant mean flux operation.*

in time in case A, whereas it initially increases and then decreases, after going through a minimum, in cases B and C. The minimum of the evolution curve is associated with the start of the relocation of the minimum concentration from y = 0 towards y = 1. This behaviour is typical of the presence of cake-enhanced concentration polarization. As the primary cause of non-uniformity is reduced (through u_w reduction), a new mechanism appears during the cake growth (i.e. cake enhanced polarization) which leads to the concentration non-uniformity evolution curves of Fig. 12. The profiles representing temporal evolution of the wall flux exhibit similar trends; i.e. the increased wall concentration non-uniformity leads to increased wall flux non-uniformity due to their relation through osmotic pressure. The transition between the decreasing and increasing non-uniformity modes is much smoother for the wall flux than for the wall concentration field.

The evolution of the membrane inlet pressure for the constant flux operation is shown in Fig. 13. The pressure increases almost linearly in time in case of Λ = 0 but the cake enhanced polarization leads to non-linear increase in cases with Λ = 50. The product concentration evolution is also shown in the same figure. There is a slight decrease of product concentration in time which is due to the increase of the mass transfer coefficient as the cross flow velocity increases in the shrinking cross section. The product concentration increases exponentially in time for the cases B and C (being quite similar for the two cases) due to the cake enhanced concentration polarization. Fig. 14 contains the same type of information as Fig. 12 but it refers to the constant flux operation. The evolution of wall flux non-uniformities is very similar to those for constant pressure, but in this case they clearly converge towards zero. The evolution of fouling layer thickness non-uniformity follows the same pattern as the one for constant pressure. However, the wall concentration non-uniformity shows a different behaviour; i.e. it is almost constant for case A, and it decreases in time for cases B and C following the reduction in wall flux and cake thickness non-uniformities. It is noted that the decrease in fractional non-uniformity in cases B and C is associated with the large values of wall concentration in those cases.

4. Concluding remarks

A mathematical model has been developed for simulating the operation of spiral wound membrane modules when organic fouling takes place. The model, comprising a system of partial differential equations in two spatial coordinates and one temporal as well as algebraic equations, is based on transversely averaged (at channel gap) quantities in both retentate and permeate sides. Three approximate closure expressions have been developed and included in the model for taking into account the fouling layer influence on (i) the pressure drop in the retentate channel, (ii) the permeation flux through the membranes, and (iii) the concentration polarization. Moreover, a recently obtained correlation (akin to a constitutive expression *applicable locally*) has been employed, linking the specific fouling resistance to permeation flux. Such expressions should be determined experimentally for particular foulants and feedwater conditions. A robust numerical algorithm has been developed to solve the system of equations, focusing on the requirement of unconditional convergence.

Several indicative results are presented in order to demonstrate the versatility of the code regarding the detailed simulation of membrane desalination operation under conditions of organic fouling. These results show that with the new model one can obtain useful insights into the various interacting mechanisms during evolution of fouling, which is impossible by using the much simpler one-dimensional models. A dynamic process simulation tool based on this model is currently employed to assess the effect of system operating variables and of the main SWM module design parameters on desalination pressure vessel performance, under realistic conditions of organic fouling. Furthermore, the presented approach will serve as the basis for the development of a very general mesoscale model of SWM module operation by incorporating appropriate sub-models accounting for particular phenomena including scaling, biofouling, particulate fouling, and interactions between them, as well as more detailed membrane transport models. Such a model can be employed to account for variation of fresh

water demand (Sassi and Mujtaba, 2013) and can be incorporated to large scale desalination plant simulators (Tula et al., 2015).

References

Avlonitis, S.A., Pappas, M., Moutesidis, K., 2007. A unified model for the detailed investigation of membrane modules and RO plants performance. Desalination 203, 218–228.

Barello, M., Manca, D., Patel, R., Mujtaba, I.M., 2015. Operation and modeling of RO desalination process in batch mode. Comput. Chem. Eng. 83, 139–156.

Cao, W., Liu, Q., Wang, Y., Mujtaba, I.M., 2016. Modelling and simulation of VMD desalination process by ANN. Comput. Chem. Eng. 84, 96–103.

Elimelech, M., Phillip, W.A., 2011. The future of seawater desalination: energy, technology and the environment. Science 333, 712–717.

Fritzmann, C., Löwenberg, J., Wintgens, T., Melin, T., 2007. State-of-the-art of reverse osmosis desalination. Desalination 216, 1–76.

Greenlee, L.F., Lawler, D.F., Freeman, B.D., Marrot, B., Moulin, P., 2009. Reverse osmosis desalination: water sources, technology, and today's challenges. Water Res. 43, 2317–2348.

Guillen, G., Hoek, E.M.V., 2009. Modeling the impacts of feed spacer geometry on reverse osmosis and nanofiltration processes. Chem. Eng. J. 149, 221–231.

Gurreri, L., Tamburini, A., Cipollina, A., G.Micale, G., Ciofalo, M., 2016. Flow and mass transfer in spacer-filled channels for reverse electrodialysis: a CFD parametrical study. J. Membr. Sci. 497, 300–317.

Hasson, D., Drak, A., Semiat, R., 2001. Inception of CaSO4 scaling on RO membranes at various water recovery levels. Desalination 139, 73–81.

Hawkins Cwirko, E., Carbonell, R.G., 1998. Transport of electrolytes in charged pores: analysis using the method of spatial averaging. J. Colloid Interface Sci. 129, 513–531.

Hoek, E.M.V., Elimelech, M., 2003. Cake-enhanced concentration polarization: a new fouling mechanism for salt rejecting membranes. Environ. Eng. Sci. 37, 5581–5588.

Hoek, E.M.V., Kim, A.S., Elimelech, M., 2002. Influence of cross flow membrane filter geometry and shear rate on colloidal fouling in reverse osmosis and nanofiltration separations. Environ. Eng. Sci. 19, 357–372.

Karabelas, A.J., Sioutopoulos, D.C., 2014. Toward improvement of methods for predicting fouling of desalination membranes—the effect of permeate flux on specific fouling resistance. Desalination 343, 97–105.

Karabelas, A.J., 2014. Key issues for improving the design and operation of spiral-wound membrane modules in desalination plants. Desalin. Water Treat. 52, 1820–1832.

Karabelas, A.J., Koutsou, C.P., Kostoglou, M., 2014. The effect of spiral wound membrane element design characteristics on its performance in steady state desalination—a parametric study. Desalination 332, 76–90.

Karabelas, A.J., Kostoglou, M., Koutsou, C.P., 2015. Modeling of spiral wound membrane desalination modules and plants—review and research priorities. Desalination 356, 165–186.

Kostoglou, M., Karabelas, A.J., 2009. On the fluid mechanics of spiral wound membrane modules. Ind. Eng. Chem. Res. 48, 10025–10036.

Kostoglou, M., Karabelas, A.J., 2012. A mathematical study of the evolution of fouling and operating parameters throughout membrane sheets comprising spiral wound modules. Chem. Eng. J. 187, 222–231.

Kostoglou, M., Karabelas, A.J., 2013. Comprehensive simulation of flat-sheet membrane element performance in steady state desalination. Desalination 316, 91–102.

Koutsou, C.P., Yiantsios, S.G., Karabelas, A.J., 2004. Numerical simulation of the flow in a plane channel containing a periodic array of cylindrical turbulence promoters. J. Membr. Sci. 231, 81–90.

Koutsou, C.P., Yiantsios, S.G., Karabelas, A.J., 2007. Direct numerical simulation of flow in spacer-filled channels: effect of spacer geometrical characteristics. J. Membr. Sci. 291, 53–69.

Koutsou, C.P., Yiantsios, S.G., Karabelas, A.J., 2009. A numerical and experimental study of mass transfer in spacer-filled channels: effects of spacer geometrical characteristics and Schmidt number. J. Membr. Sci. 326, 234–251.

Kurihara, M., Hanakawa, M., 2013. Mega-ton Water System: japanese national research and development project on seawater desalination and wastewater reclamation. Desalination 308, 131–137.

Lee, S., Elimelech, M., 2006. Relating organic fouling of reverse osmosis membranes to intermolecular adhesion forces. Environ. Sci. Technol. 40, 980–987.

Liu, Y.L., Mi, B.X., 2012. Combined fouling of forward osmosis membranes: synergistic foulant interaction and direct observation of fouling layer formation. J. Membr. Sci. 407, 136–144.

Lyster, E., Cohen, Y., 2007. Numerical study of concentration polarization in a rectangular reverse osmosis membrane channel: permeate flux variation and hydrodynamic end effect. J. Membr. Sci. 303, 140–153.

Marriott, J.I., Sorensen, E., Bogle, I.D.L., 2001. Detailed mathematical modeling of membrane modules. Comput. Chem. Eng. 25, 693–700.

Michaels, A.S., 1968. New separation technique for the CPI. Chem. Eng. Prog. 64, 31–42.

Press, W.H., Teukolsky, S.A., Vetterling, W.T., Flannery, B.P., 1992. Numerical Recipes The Art of Scientific Computing. Cambridge University Press, New York.

Ranade, V.V., Kumar, A., 2006. Fluid dynamics of spacer filled rectangular and curvilinear channels. J. Membr. Sci. 271, 1–15.

Ruth, B.F., 1946. Correlating filtration theory with industrial practice. Ind. Eng. Chem. 328, 564–571.

Sassi, K.M., Mujtaba, I.M., 2013. Optimal operation of RO system with daily variation of freshwater demand and seawater temperature. Comput. Chem. Eng. 59, 101–110.

Schafer, A.I., Fane, A.G., Waite, T.D., 1998. Nanofiltration of natural organic matter: removal, fouling and the influence of multivalent ions. Desalination 118, 109–122.

Schwinge, J., Neal, P.R., Wiley, D.E., Fletcher, D.F., Fane, A.G., 2004. Spiral wound modules and spacers: review and analysis. J. Membr. Sci. 242, 129–153.

Sioutopoulos, D., Yiantsios, S.G., Karabelas, A.J., 2010a. Relation between fouling characteristics of RO and UF membranes in experiments with colloidal organic and inorganic species. J. Membr. Sci. 350, 62–82.

Sioutopoulos, D., Karabelas, A.J., Yiantsios, S.G., 2010b. Organic fouling of RO membranes: investigating the correlation of RO and UF fouling resistances for predictive purposes. Desalination 261, 272–283.

Sioutopoulos, D.C., Goudoulas, T.B., Kastrinakis, E.G., Nychas, S.G., Karabelas, A.J., 2013. Rheological and permeability characteristics of alginate fouling layers developing on reverse osmosis membranes during desalination. J. Membr. Sci. 434, 74–84.

Tien, C., Bai, R., 2003. An assessment of the conventional cake filtration theory. Chem. Eng. Sci. 58, 1323–1336.

Tula, A.K., Eden, M.R., Gani, R., 2015. Process synthesis design and analysis using a process-group contribution method: process synthesis design and analysis using a process-group contribution method. Comput. Chem. Eng. 81, 245–259.

Vorobiev, E., 2006. Derivation of filtration equations incorporating the effect of pressure redistribution on the cake-medium interface: a constant pressure filtration. Chem. Eng. Sci. 61, 3686–3697.

Vrouwenvelder, J.S., 2009. Graf von der Schulenburg DA, Kruithof JC, Johns ML, van Loosdrecht MCM. Biofouling of spiral-wound nanofiltration and reverse osmosis membranes: a feed spacer problem. Water Res. 43, 583–594.

Wang, X.L., Tsury, T., Nakao, S., Kimura, S., 1995. Electrolyte transport through nanofiltration membranes by the space charge model and comparison with Teorell-Meyer-Sievers model. J. Membr. Sci. 103, 117–133.

Wang, J.W., Dlamini, D.S., Mishra, A.K., Pendergast, M.T.M., Wong, M.C.Y., Mamba, B.B., Freger, V., Verliefde, A.R.D., Hoek, E.M.V., 2014. A critical review of transport through osmotic membranes. J. Membr. Sci. 454, 516–537.

Ye, Y., Le Clech, P., Chen, V., Fane, A.G., Jefferson, B., 2005. Fouling mechanisms of alginate solutions as model extracellular polymeric substances. Desalination 175, 7–20.

Yiantsios, S.G., Sioutopoulos, D., Karabelas, A.J., 2005. Colloidal fouling of RO membranes: an overview of key issues and efforts to develop improved prediction techniques. Desalination 183, 257–272.